

Stepwise Hierarchical Self-Assembly of Supramolecular Amphiphiles into Higher-Order Threedimensional Nanostructures

Flavio della Sala, Wessel Verbeet, Simone Silvestrini, Ilaria Fortunati, Camilla Ferrante and Leonard J. Prins*

Abstract: Hierarchical self-assembly describes the spontaneous formation of large well-defined molecular structures through a sequence of spontaneous processes driven by noncovalent interactions between molecules and intermediate structures. The chemical information embedded in the initial molecules determines the structural outcome of the overall assembly process. This is clearly advantageous in terms of product accessibility, but poses limits to the extent of control that can be exerted over the process. Here we report the stepwise hierarchical self-assembly of well-defined three-dimensional organic nanostructures with dimensions of over 100 nm in each single xyz-direction and a total volume of up to $1.5 \times 10^{-2} \mu\text{m}^3$. These structures are formed through three consecutive processes that rely exclusively on the establishment of noncovalent interactions between the components: (1) complex formation between Zn^{2+} and a macrocyclic ligand, (2) association of the amphiphiles in disk-like micellar structures and, finally, (3) ATP-induced stacking of the disks into large hexagonal prisms. The top and bottom surface of these structures are flat multivalent cationic surfaces covered with ATP with dimensions in the order of $2 \times 10^5 \text{ nm}^2$ onto which nanometer-sized gold nanoparticles can be deposited through a final self-assembly process. The stepwise hierarchical process bears a close analogy with a multistep covalent synthetic pathway with the difference that all steps rely exclusively on noncovalent interactions.

Introduction

Over the past decades, self-assembly has emerged as the most attractive tool to prepare molecular structures of nano-sized dimensions.^[1,2] Self-assembly relies on the spontaneous organization of molecules in structures through the development of noncovalent interactions. Self-assembly has also been referred to as noncovalent synthesis^[3,4] to underline the analogy with classical covalent synthesis, which relies on the formation of covalent bonds to make new molecules. Hierarchical self-assembly is said to occur in case the initial assemblies spontaneously further assemble into new structures of higher order through the installment of additional noncovalent interactions.^[5,6] This has turned out to be a very fruitful approach to obtain structures, which may even reach dimensions in the

order of micrometers, with exciting materials properties.^[7,8] Although it is tempting to make an analogy between hierarchical self-assembly and a multi-step covalent synthetic pathway, it is difficult to sustain such an analogy. A key characteristic of hierarchical self-assembly is that all information leading to the final structure is already embedded in the initial molecular components and the entire process is a spontaneous one. This marks a strong difference with a multistep covalent synthesis, which is a stepwise process. Our ability to design synthetic pathways that rely on the controlled activation of consecutive self-assembly processes is very limited, despite the fact that this would provide an access route with unprecedented control to molecular nanostructures of different structure and dimension.

Here, we present a multistep self-assembly process that involves a series of consecutive processes relying on noncovalent interactions only. Each step yields a well-defined and reproducible structure and activation through the addition of further compounds is required to proceed with the next step (Figure 1). The process starts with the formation of a metallo-surfactant through the complexation of a Zn^{2+} -ion by the amphiphile, which then self-assemble in disk-like micelles. Upon addition of adenosine 5'-triphosphate (ATP), these disks stack on top of each other as a result of electrostatic interactions forming extraordinary large 3D hexagonal prisms with dimensions of over 100 nm in each single xyz-direction and a total volume of up to $1.5 \times 10^{-2} \mu\text{m}^3$. Eventually, these stacked disks can be decorated with negatively charged gold nanoparticles (Au NPs) through a final self-assembly process after activating the stacked disks with an enzyme.

Results and Discussion

Self-assembly of $\text{C}_{20}\text{TACN-Zn}^{2+}$ in disk-like micelles

As principal component of our studies we focused on the use of amphiphiles, because this class of compounds gives access to a large variety of structurally diverse assemblies^[9–13] with applications in nanodevices,^[14–16] drug delivery,^[17,18] catalysis,^[19,20] and for the templated synthesis of inorganic structures.^[21] Despite the potentially large structural diversity, spherical micelles and vesicles are the most abundant self-assembled systems.^[12,22] On the other hand, non-spherical assemblies are usually achieved by means of copolymers,^[10] that allow shape control^[18] thanks to the ability to balance their hydrophilic and hydrophobic properties^[23–25] in a predictable manner.^[26,27] Elegant supramolecular self-assembly processes with small and non-polymeric building blocks have also been reported,^[28–30] some of which having a non-spherical structure.^[31–40]

[*] Dr. F. della Sala, W. Verbeet, Dr. S. Silvestrini, Dr. I. Fortunati, Prof. Dr. C. Ferrante, Prof. Dr. L. J. Prins
Department of Chemical Sciences, University of Padova
Via Marzolo 1, 35131 Padova (Italy)
E-mail: leonard.prins@unipd.it

Supporting information for this article is given via a link at the end of the document. ((Please delete this text if not appropriate))

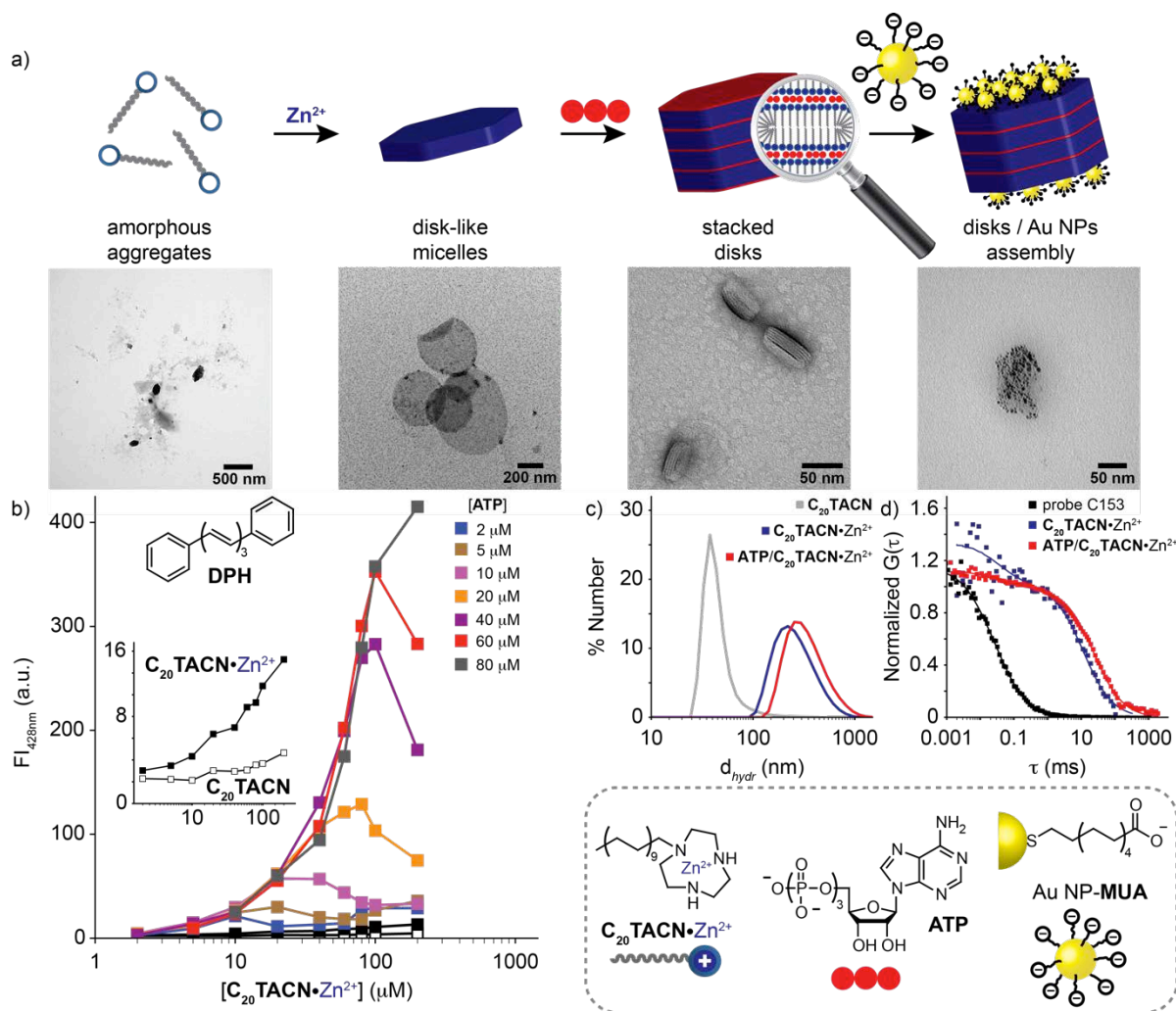


Figure 1. Stepwise hierarchical self-assembly. a) $C_{20}TACN$ (100 μM) undergoes hierarchical self-assembly in the presence of, respectively, Zn^{2+} -ions (100 μM), **ATP** (20 μM) and Au NP-MUA (20 μM in terms of NP-bound ligand) and corresponding TEM micrographs. b) Fluorescence intensity (FI) at 428 nm as a function of the concentration of $C_{20}TACN \cdot Zn^{2+}$ (2–200 μM) added to an aqueous buffer solution with different concentrations of **ATP** (2–80 μM) in the presence of **DPH** (2 μM , $\lambda_{ex} = 355$ nm, slit_{ex/em} = 5/5 nm) as the fluorescence probe. Control experiments: titration of $C_{20}TACN$ only (no Zn^{2+} , empty squares) and of $C_{20}TACN \cdot Zn^{2+}$ only (no **ATP**, black squares). c) DLS analysis of $C_{20}TACN$ (100 μM , gray), $C_{20}TACN \cdot Zn^{2+}$ (100 μM , blue) and **ATP**/ $C_{20}TACN \cdot Zn^{2+}$ (20/100 μM , red). d) Normalized FCS curves of probe C153 in HEPES solution (100 nM, black), with $C_{20}TACN \cdot Zn^{2+}$ (100 μM , blue) and **ATP**/ $C_{20}TACN \cdot Zn^{2+}$ (20/100 μM , red). Solid lines are fitting traces. General conditions: HEPES (5 mM, pH 7.0), 25 °C.

We recently reported that the addition of **ATP** to a solution of the amphiphile $C_{16}TACN \cdot Zn^{2+}$ causes the formation of vesicles, which can be used as nanoreactors for a chemical reaction.^[41] **ATP** stabilizes the structure through multipoint electrostatic interactions between the phosphate groups and the 1,4,7-triazacyclononane (**TACN**)· Zn^{2+} head groups. In the presence of an **ATP**-cleaving enzyme, transient stability of the assemblies was observed because the waste products of **ATP** hydrolysis (AMP + 2 P_i) cannot stabilize the vesicles. In an attempt to increase the kinetic stability of the vesicles, we decided to synthesize the new amphiphile $C_{20}TACN$ in which the hydrophobic chain is elongated by 4 carbon atoms (Scheme S1). It is known that this reduces the dissociation rate of surfactants from the aggregates,^[42] and for that reason we expected this modification to increase the kinetic stability of the vesicles after

hydrolysis by the enzyme. The aggregation behavior of the free ligand $C_{20}TACN$ (i.e. without Zn^{2+} , Figure 1b inset) was first studied with fluorescence spectroscopy using 1,6-diphenyl-1,3,5-hexatriene (**DPH**, $\lambda_{ex} = 355$ nm, $\lambda_{em} = 428$ nm) as a probe testing the presence of apolar compartments in aggregates.^[43] The amphiphile $C_{20}TACN$ was diluted from a concentrated millimolar stock solution to the desired final concentration in the presence of **DPH** (2 μM) and the fluorescence intensity (FI) was measured as a function of time (Figure S1). At none of the concentrations of $C_{20}TACN$ studied (2–200 μM , Figure 1b, white squares) we observed an evident increase in FI, which would have been indicative of the presence of a critical aggregation concentration (*cac*) above that aggregates formed. Although dynamic light scattering (DLS) measurements suggested the presence of relatively small aggregates (Figure 1c), TEM images

obtained after staining an evaporated drop of a **C₂₀TACN** solution (100 μM , [HEPES] = 5 mM, pH 7.0) with uranyl acetate solution (2%) showed just amorphous aggregates (Figure 1a). Based on these observations, it was concluded that **C₂₀TACN** in its free ligand form does not self-assemble into well-defined structures.



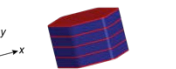
Different observations were made for **C₂₀TACN·Zn²⁺**, obtained simply by adding 1 equivalent of $\text{Zn}(\text{NO}_3)_2$ to a solution of **C₂₀TACN** (Figure 1b, *black squares*). Fluorescence titrations in the presence of **DPH** (2 μM) gave slightly higher values compared to those observed for **C₂₀TACN**, but, nonetheless, neither in this case a clear evidence of the presence of a *cac* emerged from this titration. Yet, different information emerged from other analytical techniques. Surface tension analysis of equilibrated solutions of **C₂₀TACN·Zn²⁺** at different concentrations in aqueous buffer at pH 7.0 ([HEPES] = 5 mM) revealed the formation of aggregates with a *cac* of around 46 μM (Figure S2). The presence of stable aggregates at a concentration of 100 μM , *i.e.* above the *cac*, was confirmed by DLS measurements that gave a hydrodynamic diameter of 268 ± 87 nm (Figure 1c). Fluorescence correlation spectroscopy (FCS) analysis supported the DLS measurements (Figure 1d). Using the signal component assigned to the probe (C153) embedded into the hydrophobic compartment of the assemblies, τ_{D_2} , an average hydrodynamic diameter of 270 ± 74 nm was calculated. Importantly, structural analysis by TEM revealed that **C₂₀TACN·Zn²⁺** (100 μM) self-assembles in well-defined flat disk-like structures with a relative broad size distribution ($d_{\text{avg}} = 185 \pm 98$ nm, Figures 2a and S3–S5). Although this kind of flat structures are well known and referred to as bicelles, the remarkable feature of this system is that the structures are formed from a single amphiphile^[44] and not from a mixture. It is interesting to note that some of the disk-like structures had a hexagonal shape which could be indicative of the packing arrangement of **C₂₀TACN·Zn²⁺** amphiphiles in the assembly.^[45] A confirmation for the formation of flat structures was obtained from cryo-EM images obtained from the same solution (Figures 2b and S8). Finally, atomic force microscopy (AFM) of **C₂₀TACN·Zn²⁺** deposited on a SiO_2 -surface showed the formation of flat assemblies with an average layer thickness of around 5.3 nm, which is consistent with a partly interdigitated bilayer structure (Figure 2c, the fully elongated form of **C₂₀TACN·Zn²⁺** has a length of ~ 2.8 nm). Our hypothesis for the inability of **DPH** to detect a *cac* is based on the intrinsic fluorescence properties of this probe. As reported in the literature,^[46] **DPH** is a rod-shaped molecule whose fluorescence quantum yield and lifetime do not change upon insertion in lipid bilayers. **C₂₀TACN·Zn²⁺** is organized in densely packed bilayers with low membrane fluidity. The firmly packed non-polar chains of **C₂₀TACN·Zn²⁺** can prevent incorporation of **DPH** inside the disk-like aggregates explaining the low FI values measured.

Stacking of the **C₂₀TACN·Zn²⁺** disks in the presence of ATP

Considering that addition of **ATP** to a solution of **C₁₆TACN·Zn²⁺** induced vesicle formation,^[41] we were interested in studying the effect of **ATP** on the aggregation behavior of **C₂₀TACN·Zn²⁺**. The first indication that the self-assembly of **C₂₀TACN·Zn²⁺** (100 μM) is affected by **ATP** came from fluorescence titrations in which the concentration of **C₂₀TACN·Zn²⁺** was gradually increased in the presence of fixed amounts of **ATP** (2–80 μM) and **DPH** (2 μM , Figure 1b). Also in this case a time-dependent FI was observed, but the FI stabilized at significantly higher values together with a remarkable decrease of the *cac* regardless the amount of **ATP** present (<5 μM , Figure S9). Compared to the same titration in the absence of **ATP** (see above), an increase in FI (at equilibrium) was observed for all samples even at low micromolar concentrations. It was further observed that, for all concentrations of **ATP**, a maximum value of the FI was obtained when a [ATP]/[**C₂₀TACN·Zn²⁺**] ratio of around 1:3 was reached, followed by a moderate decrease at higher surfactant concentrations. The fact that in this case the FI of **DPH** is sensitive to the formation of aggregates indicates that the interaction of **ATP** with the **TACN·Zn²⁺** head groups decreases the packing density of the bilayer causing a higher fluidity of the membrane, and therefore facilitating incorporation of **DPH** in the aggregate structure.

Interestingly, rather than causing a structural change in the surfactant assembly as observed previously for the **C₁₆TACN·Zn²⁺** surfactant,^[41,47] TEM analysis revealed that the addition of **ATP** caused a stacking of the disks and thus adds a new level of self-organization to the system (Figure 1a). Although stacks were observed for all ratios of **ATP:C₂₀TACN·Zn²⁺** studied (1:0.2–1:25, Figures S10–S16), the optimal results were obtained for [**C₂₀TACN·Zn²⁺**] = 100 μM and [ATP] = 20 μM at which well-defined circular/hexagonal stacked disks were detected (Figures 3a,b and S12). The absence of **ATP**-induced structural changes in the disks is suggested by the comparable mean size estimated from the TEM images of the disks formed by **C₂₀TACN·Zn²⁺** alone and in the presence of **ATP** (185 ± 98 and 242 ± 118 nm, respectively). We estimated a

Table 1. Summary of the average size of **C₂₀TACN**, **C₂₀TACN·Zn²⁺** and **ATP/C₂₀TACN·Zn²⁺** as calculated by DLS, cryo-EM and FCS analyses.

	 C₂₀TACN (nm)	 C₂₀TACN·Zn²⁺ (nm)	 ATP/C₂₀TACN·Zn²⁺ (nm)
DLS	57 ± 15	268 ± 87	347 ± 49
cryo-EM	– ^a	(xy) 185 ± 98 ^b	(xy) 480 ± 200 ^c (z) 224 ± 91
FCS	– ^a	270 ± 74	530 ± 160

[a]: Analysis not performed with amorphous aggregates. [b]: As calculated from TEM analysis. [c]: Mean size calculated from TEM analysis: 242 ± 118 nm.

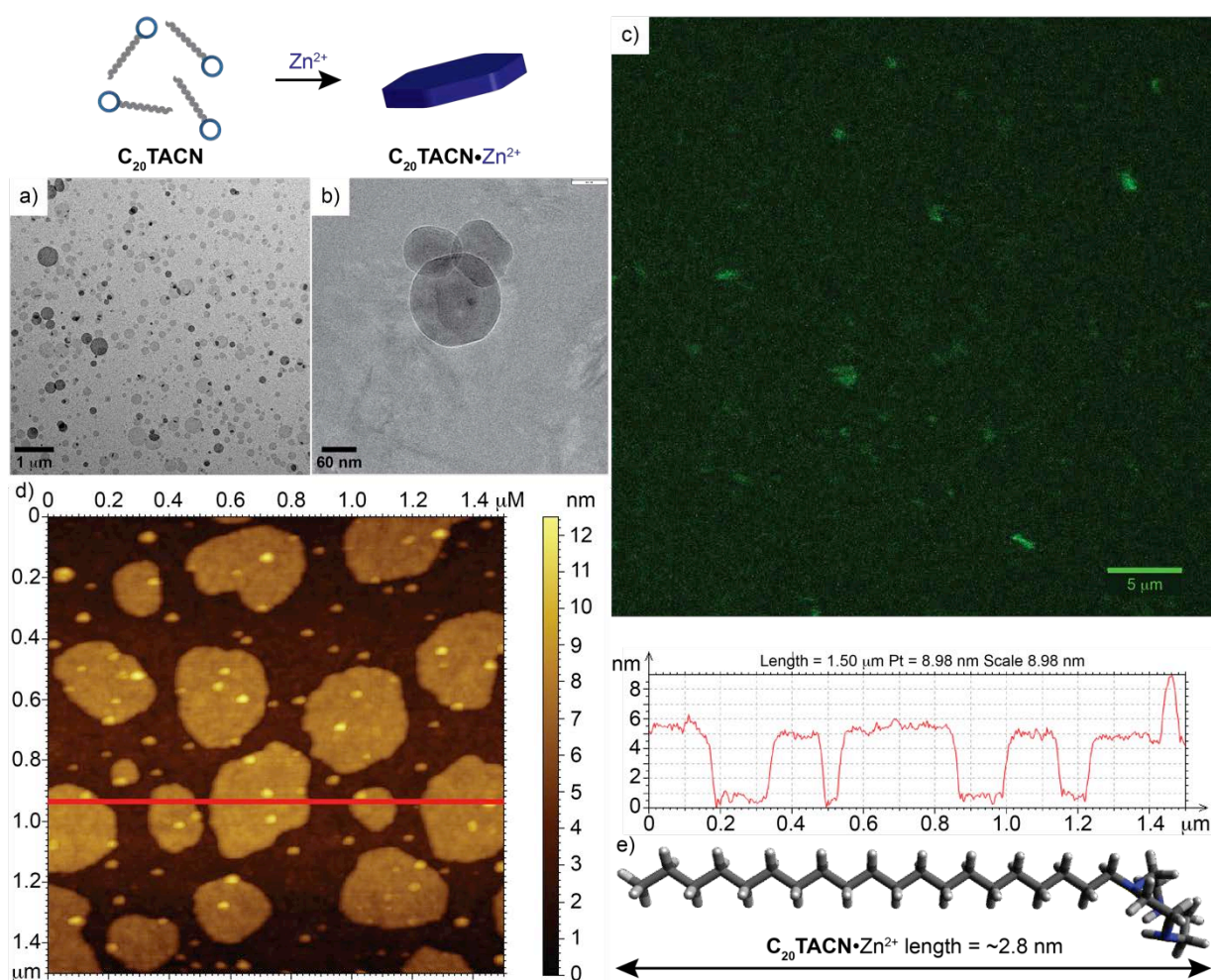


Figure 2. Characterization of disk-like micelles formed by C_{20}TACN in the presence of Zn^{2+} -ions. a): TEM image of $[\text{C}_{20}\text{TACN}\cdot\text{Zn}^{2+}] = 100 \mu\text{M}$ (stained with 2% uranyl acetate solution). Scale bar: $1 \mu\text{m}$. b) Cryo-EM image (same conditions of a). Scale bar: 60 nm . c): Confocal image in the presence of C153 ($1 \mu\text{M}$) under 400 nm excitation. d) Topographic AFM image of $[\text{C}_{20}\text{TACN}\cdot\text{Zn}^{2+}] = 500 \mu\text{M}$ aqueous solution casted on a SiO_2 plate. The red line indicates the thickness of the disk-like micelles ($\sim 6 \text{ nm}$). e): Estimated length of fully extended $\text{C}_{20}\text{TACN}\cdot\text{Zn}^{2+}$.

layer thickness of $3.6 \pm 0.4 \text{ nm}$ (Figure 3b), consistent with stacked bilayers that have undergone partial intercalation of the apolar chains.^[28] Cryo-EM studies showed that the **ATP**-induced stacks may assume dimensions in the z-direction of up to 400 nm indicating that a single stack may contain over hundred disks (Figure 3e). Information on the kinetics of the stacking process was obtained from TEM-analysis of aliquots taken from a solution of $\text{C}_{20}\text{TACN}\cdot\text{Zn}^{2+}$ ($100 \mu\text{M}$) at time zero, 1 h , 5 h , and 24 h after adding **ATP** ($20 \mu\text{M}$, Figure S18). At time zero, surfactants are organized in amorphous, globular aggregates as seen by both TEM and cryo-EM which is in line with previous studies on the self-assembly of $\text{C}_{20}\text{TACN}\cdot\text{Zn}^{2+}$ which had indicated that it took around 1 h for $\text{C}_{20}\text{TACN}\cdot\text{Zn}^{2+}$ to self-assemble in disks. Indeed, in the presence of **ATP**, stacked two- or three-layered disks are already visible after 1 hour . After 5 hours , the disks keep on improving their homogeneity and longer stacks are observed until a thermodynamically stable state is reached after around 24 hours . Cryo-EM confirmed the

formation of the stacked disks, some of which with a well-defined hexagonal shape (Figures 3e,f and S17). Two control experiments provided evidence that **ATP** is intimately intercalated between the $\text{C}_{20}\text{TACN}\cdot\text{Zn}^{2+}$ disks resulting in a surprising robustness of the entire structure. After allowing the formation of the $\text{ATP}/\text{C}_{20}\text{TACN}\cdot\text{Zn}^{2+}$ stacked disks ($20/100 \mu\text{M}$, respectively), we induced precipitation of the assemblies by vigorous ultracentrifugation. A strong decrease of the **ATP** absorbance maximum at 260 nm showed that a relevant amount of **ATP** was removed from the solution (Figure S21). Further confirmation was obtained by testing the **ATP** stability under hydrolytic conditions installed by the presence of potato apyrase, an enzyme that hydrolyses **ATP** into adenosine 5'-monophosphate (AMP) and two molecules of orthophosphate P_i .^[41,48] **ATP** ($20 \mu\text{M}$) was added to a pre-equilibrated solution of $\text{C}_{20}\text{TACN}\cdot\text{Zn}^{2+}$ disks and **DPH** ($2 \mu\text{M}$) in the presence or absence of potato apyrase (1.5 U mL^{-1} , $[\text{CaCl}_2] = 0.25 \text{ mM}$, $37 \text{ }^\circ\text{C}$) and the FI intensity was measured as a function of time.

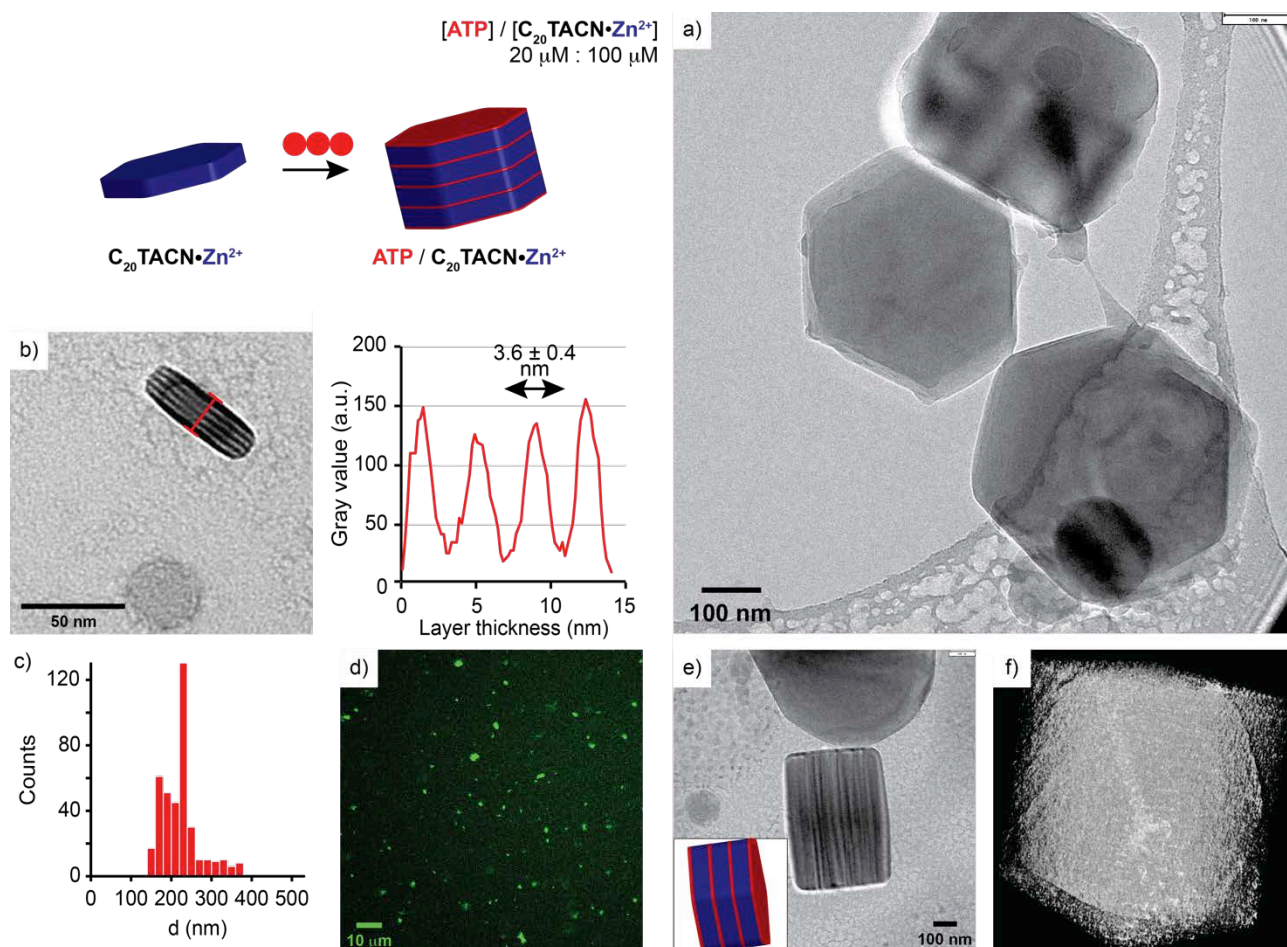


Figure 3. Stacking of the $C_{20}TACN-Zn^{2+}$ in the presence of ATP. a) TEM image of the formation of stacked disks of $C_{20}TACN-Zn^{2+}$ in the presence of ATP (scale bar: 100 nm). b) Representative example of the stacked layers (thickness = 3.6 ± 0.4 nm obtained from around 100 counts) on a vertically-positioned hexagonal polyhedron (scale bar: 50 nm). c) Size distribution of a representative batch of $ATP/C_{20}TACN-Zn^{2+}$ (242 ± 118 nm, as estimated by TEM). Only aggregates oriented with the hexagonal face positioned on the surface were selected. d) Confocal image in the presence of C153 (1 μ M) under 400 nm excitation. e) Representative cryo-EM image and (f) corresponding tomogram showing the 3D hexagonal polyhedron. Scale bars: 100 nm. Experimental conditions: $C_{20}TACN-Zn^{2+}$ (100 μ M), ATP (20 μ M), HEPES (5 mM, pH 7.0), 25 $^{\circ}$ C

Comparison of the two samples showed that, under dissipative conditions, the FI intensity decreased only very slowly over the time course of hours indicating a very high stability of the stacked disks. The result was rather surprising considering our previous study on ATP-stabilized vesicles composed of $C_{16}TACN-Zn^{2+}$, which had lifetimes in the order of minutes under similar conditions.^[41] This indicates that ATP is hardly accessible as substrate for the enzyme, in line with the postulation that ATP is intercalated between $C_{20}TACN-Zn^{2+}$ disks. It is further noticed that the addition of AMP (20 μ M) and P_i (40 μ M) under the same conditions did not cause a significant increase in FI (Figure S22).

Self-assembly of gold nanoparticles on the $ATP/C_{20}TACN-Zn^{2+}$ stacked disks

The stacked disks are well-defined structures of extraordinary large dimensions especially considering that they are made up entirely of organic material. This, combined with a very high stability, gives the unique possibility to use these structures as

robust organic platforms for the spatial organization of additional functional elements, which may have large dimensions by themselves. Particularly attractive are the top and bottom of the $ATP/C_{20}TACN-Zn^{2+}$ stacked disks, which are flat organic surfaces with an average surface area of around 3×10^4 nm² (using a radius of the hexagonal faces of around 120 nm). The overall volume of the structure is around 1.5×10^{-2} μ m³. This is an enormous size, not only compared to that of molecules, but also to that of materials with nano-sized dimension (10–100 nm). Over the past decades nanoparticles (NPs) have emerged as highly efficient components of innovative chemical systems for application in the fields of catalysis, diagnostics and materials science.^[49,50] Examples of arrays of NPs on 2D surfaces are available for electronic, optical and sensing applications.^[51–54] We therefore decided to explore the possibility of assembling NPs on the surface of the stacked disks. These surfaces are covered with a large number of ATP molecules noncovalently bound to the $TACN-Zn^{2+}$ head groups, but, as the stability

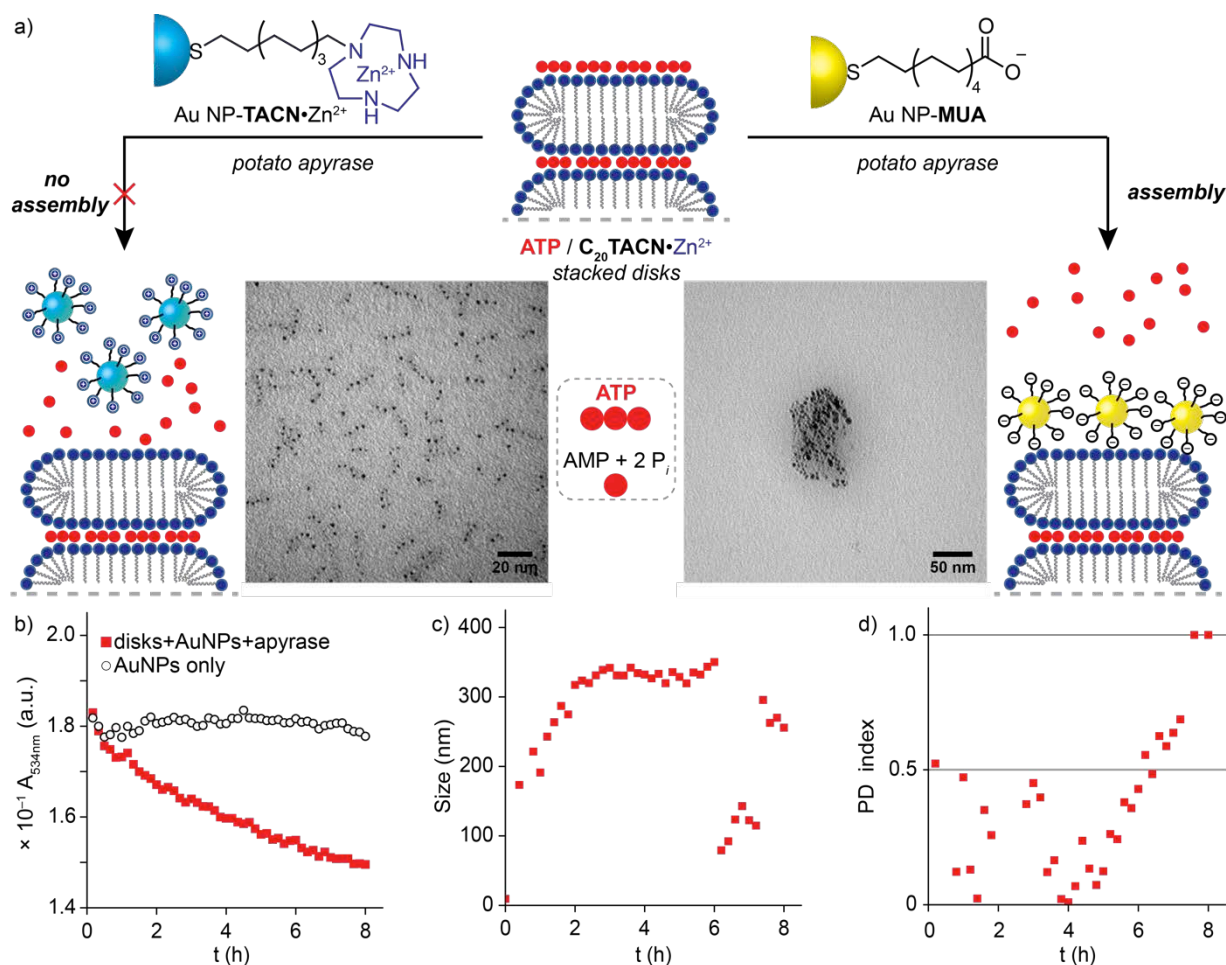


Figure 4. Self-assembly between the $\text{ATP/C}_{20}\text{TACN}\cdot\text{Zn}^{2+}$ stacked disks and Au NP-MUA in the presence of potato apyrase. a) The enzyme cleaves the outer layer of ATP into AMP and 2P_i , exposing the positively charged assembly surface for a further level of functionalization. In buffered environment, Au NP-MUA is negatively charged and adsorbed on the surface of the stacked disks (right). Conversely, the self-assembly does not occur in the presence of Au NP-TACN-Zn²⁺ because of electrostatic repulsion (left). Experimental conditions: $\text{C}_{20}\text{TACN}\cdot\text{Zn}^{2+}$ (100 μM), ATP (20 μM), HEPES (5 mM, pH 7.0), potato apyrase (1.5 U mL⁻¹), CaCl_2 (0.25 mM), Au NP-MUA or Au NP-TACN-Zn²⁺ (20 μM , in terms of NP-bound ligand), 37 °C. TEM scale bar: 20 nm (left), 50 nm (right). b) Representative kinetic profile monitored by UV/Vis spectroscopy. Red squares: Au NP-MUA (20 μM), $\text{ATP/C}_{20}\text{TACN}\cdot\text{Zn}^{2+}$ (20/100 μM), potato apyrase (1.5 U mL⁻¹). White circles: Au NP-MUA (20 μM). c, d) Representative kinetic profile monitored by DLS analysis: Au NP-MUA (20 μM), $\text{ATP/C}_{20}\text{TACN}\cdot\text{Zn}^{2+}$ (20/100 μM), potato apyrase (1.5 U mL⁻¹). All the experiments were performed in a buffered aqueous solution (5 mM HEPES, pH 7.0) with CaCl_2 (0.25 mM) at 37 °C.

studies in the presence of enzyme demonstrated, these can be hydrolyzed without affecting the overall structural stability of the stacked disks, but exposing a large positively charged surface (Figures S21,22). We reasoned that monolayer-protected gold NPs with negatively charged head groups would bind to the surface due to the formation of multivalent electrostatic interactions. We therefore prepared Au NPs stabilized by 11-mercaptopundecanoic acid (Au NP-MUA, $d_{\text{avg}} = 3.1 \pm 0.8$ nm) by adopting a slightly modified procedure developed by Stucky and co-workers (Figures S23,24).^[55]

As control, we used Au NP-TACN-Zn²⁺ which are Au NPs stabilized by a monolayer of alkanethiols bearing cationic TACN-Zn²⁺ as head groups. Au NP-TACN-Zn²⁺ has been extensively used by our group for sensing and catalysis

applications.^[56] $\text{ATP/C}_{20}\text{TACN}\cdot\text{Zn}^{2+}$ (20/100 μM) stacked disks were incubated with potato apyrase (1.5 U mL⁻¹, $[\text{CaCl}_2] = 0.25$ mM, 37 °C) overnight. Cryo-EM confirmed that the hexagonal stacked disks are preserved after treatment with only the enzyme or CaCl_2 (Figures 25,26). We then split the batch in two aliquots and added either Au NP-MUA or Au NP-TACN-Zn²⁺ (20 μM in terms of head group concentration). For these samples, TEM analysis was performed without uranyl acetate stain in order to have better contrast for the correct localization of the Au NPs. We observed that MUA-stabilized Au NPs were clustered in very precise regions of the TEM grid (Figures 4a, right and S27–S34). The dimensions of these clusters are comparable with that of the $\text{ATP/C}_{20}\text{TACN}\cdot\text{Zn}^{2+}$ stacked disks. On the contrary, TACN-Zn²⁺-stabilized Au NPs were randomly

distributed over the entire surface of the TEM grid, confirming that not only the electrostatic repulsion between Au NP-TACN·Zn²⁺ and the ATP/C₂₀TACN·Zn²⁺ disks prevents self-assembly (Figure 4a, left and S36,37) but also that partial degradation of stacked disks occurs as evidenced by the increased irregularity of the perimeter of the assemblies (Figures S36,37). The removal of ATP caused by the presence of the enzyme is crucial for the successful interaction of Au NP-MUA with the stacked disks. Control experiments revealed that, in the absence of potato apyrase, Au NP-MUA undergoes limited and unspecific interaction with the stacked disks only at high NP concentration ([MUA] = 200 μM, Figure S28).

Further evidence for the self-assembly of Au NP-MUA on the surface of ATP/C₂₀TACN·Zn²⁺ stacked disks was obtained from UV/Vis and DLS analyses (Fig. 4b–d). Au NP-MUA by itself forms a stable homogeneous solution as evidenced by the absence of any changes in the absorption peak intensity at 534 nm over a period of 8 h (Fig. 4b). On the other hand, kinetic measurements revealed a slow decrease in absorption over the same time period when Au NP-MUA was added to a solution containing the stacked disks ATP/C₂₀TACN·Zn²⁺ in the presence of enzyme. The decrease occurred over the entire wavelength indicating that slow aggregation was at the basis of this observation. This was confirmed by DLS measurements in which the instrument was set to follow the scattering of light by the nanoparticles (Fig. 4c). It is noted that each point has been recorded with a fixed attenuation factor. This means that the scattering analysis becomes unreliable if there are too few assemblies in solution. We monitored in time the variation of the hydrodynamic size and the polydispersity (PD) index of a solution containing the stacked disks (ATP/C₂₀TACN·Zn²⁺ 20/100 μM), potato apyrase (1.5 U mL⁻¹, [CaCl₂] = 0.25 mM, 37 °C) to which Au NP-MUA (20 μM) was added. Within two hours the hydrodynamic diameter increased from around 10 nm (the size of Au NP-MUA) to around 330 nm, consistent with the size of the aggregates, which indicates the association of Au NPs to the stacked disks. For the subsequent 4 h, the size remained stable at ~330 nm, after which the system started to precipitate as evidenced by the dramatic increase in the PD index (Fig. 4d).

Conclusions

Here we have demonstrated the stepwise self-assembly of well-defined tridimensional organic structures of extraordinary large dimensions. The pathway towards structure formation relies on three consecutive processes that rely exclusively on the establishment of noncovalent interactions between the components: (1) complex formation between Zn²⁺ and a macrocyclic ligand, (2) association of the amphiphiles in disk-like micellar structures and, finally, (3) ATP-induced stacking of the disks into large three-dimensional objects. The final structures have dimensions of over 100 nm in each single xyz-direction and reach a total volume of up to $1.5 \times 10^{-2} \text{ cm}^3$. The top and bottom surface of these structures are flat multivalent cationic surfaces covered with ATP with dimensions in the order of $2 \times 10^5 \text{ nm}^2$. These surfaces can be activated by adding the enzyme

potato apyrase, which converts ATP in the weak affinity ligands AMP and 2 P_i. It was shown that negatively charged Au NPs can then be deposited on these surfaces through a final self-assembly process.

Overall, a protocol has been developed that exploits the hierarchical self-assembly of molecular components into large molecular structures. At difference with previous examples, after each step the systems needs to be activated in order for successive self-assembly to occur. This makes for a close analogy with a multi-step covalent synthetic pathway with the difference that all steps rely exclusively on noncovalent interactions. The strategy permits the straightforward formation of large well-defined organic objects that can be used for the spatial organization of nanometer-sized gold nanoparticles. These hybrid inorganic-organic systems may find use in applications that require the close proximity of nanoparticles, such as in sensing or (tandem) catalysis.

Experimental Section

General. All commercially available reagents were used as received. Fluorophores 1,6-diphenyl-1,3,5-hexatriene (DPH) and coumarin153 (C153) were purchased from Sigma-Aldrich and Exciton, respectively, and were used without further purification. The enzyme potato apyrase (PA) was obtained from Sigma Aldrich and used without further purification. In particular, PA was dissolved in 1.0 mL of mQ-water and divided in 20 working aliquots of 50 μL with a concentration of 100 U mL⁻¹ and preserved at -20 °C. The Zn(NO₃)₂-stock solution was standardized using EDTA following standard procedures. The buffer 4-(2-hydroxyethyl)-1-piperazineethanesulfonic acid (HEPES) was purchased from Sigma-Aldrich and used without further purification. Nucleotides ATP and AMP were purchased from Sigma-Aldrich and their stock solutions were prepared both by weight and UV/Vis spectroscopy using the molar extinction coefficients: ϵ_{259} (ATP, AMP) = 15400 M⁻¹ cm⁻¹. UV/Vis spectra were measured on a Varian Cary50 spectrophotometer equipped with thermostatted multiple cell holders. Fluorescence measurements were performed on a Varian Cary Eclipse fluorescence spectrophotometer also equipped with a thermostatted cell holder. Dynamic light scattering (DLS) analysis was performed on a Malvern Zetasizer Nano-S instrument. ESI-MS mass spectra were obtained with an Agilent Technologies LC/MSD Trap SL mass spectrometer. The high-resolution mass spectrum (HRMS) was recorded on a Mariner Biosystem (API-TOF) mass spectrometer. NMR spectra were recorded using a Bruker AV III 500 spectrometer operating at 500 MHz for ¹H and at 126 MHz for ¹³C. Multiplicity is given as follow: s=singlet, d=doublet, t=triplet, m=multiplet, br=broad peak. Thermogravimetric analysis (TGA) was performed on ~1 mg nanoparticle sample using a QR5000 IR model TA instrument using a temperature gradient from 100 to 1000 °C under a continuous air flow.

Synthesis and characterization of C₂₀TACN. 1,4-Di(*tert*-butyl)carboxylate-1,4,7-triazacyclononane (**1**). A solution of 2-(Boc-oxyimino)-2-phenylacetone nitrile (3.80 g, 1.55 mmol) in anhydrous CHCl₃ (15 mL) was added with a syringe pump (1 mL h⁻¹) to a solution of 1,4,7-triazacyclononane (1.00 g, 7.70 mmol) and Et₃N (3.2 mL, 23.2 mmol) in CHCl₃ (40 mL). The reaction mixture was stirred for 20 h at rt. The organic phase was then washed with 5% aqueous Na₂CO₃ (3x10 mL), brine (2x20 mL), and 10% aqueous citric acid (3x10 mL). The organic phase was dried over MgSO₄ and the solvent was removed under reduced pressure. Pure compound **1** (1.11 g, 44%) was obtained as pale yellow oil. Spectral data is in agreement with the literature.^[57,58] ¹H NMR

(CDCl₃, 500 MHz, 298 K): δ 1.41 (s, 18 H, 6xCH₃), 2.06 (bs, 1H, NH), 2.86–2.87 (m, 4H, 2xCH₂N), 3.18–3.23 (m, 4H, 2xCH₂N), 3.36–3.42 (m, 4H, 2xCH₂N) ppm. ¹³C NMR (CDCl₃, 126 MHz, 298 K): δ 28.5, 47.3, 47.7, 48.1, 48.2, 49.5, 49.8, 50.37, 50.43, 51.4, 52.1, 52.3, 52.9, 79.7, 79.8, 155.8, 156.0 ppm. MS (ES⁺) m/z calculated for C₁₆H₃₁N₃O₄ [M+H]⁺ 330.2, found 330.3.

1-Eicosyl-4,7-bis(tert-butoxycarbonyl)-1,4,7-triazacyclononane (2).

Compound **1** (534 mg, 1.62 mmol) and 1-bromoeicosane (763 mg, 2.11 mmol) were dissolved in MeCN (40 mL) containing Na₂CO₃ (409 mg, 4.87 mmol). The mixture was heated at 60 °C overnight. Then, the solvent was removed under reduced pressure and the crude product was purified by flash chromatography (SiO₂, MeOH/CH₂Cl₂ 3:97 to 1:10). Compound **2** was obtained as a pale yellow oil (843 mg, 85%). ¹H NMR (CDCl₃, 500 MHz, 298 K): δ 0.87 (t, *J* = 6.9 Hz, 3H, CH₃), 1.25 (s, 34H, CH₂), 1.51 (m, 18H, 6xCH₃), 1.66 (s, 2H, CH₂), 2.46 (s, 2H, CH₂N), 2.59 (s, 4H, 2xCH₂N), 3.15 (s, 4H, 2xCH₂N), 3.47 (m, 4H, 2xCH₂N) ppm. ¹³C NMR (CDCl₃, 126 MHz, 298 K): δ 14.3, 22.8, 28.6, 29.5, 29.6, 29.7, 29.9, 31.1, 32.1, 33.0, 34.2, 53.5, 53.7, 76.9, 77.1, 77.4, 79.5, 155.6 ppm. HRMS (ES⁺) m/z calculated for C₃₆H₇₂N₃O₄ [M+H]⁺ 610.5517, found 610.5534.

1-Eicosyl-1,4,7-triazacyclononane (C₂₀TACN). Compound **2** (843 mg, 1.38 mmol) was dissolved in a mixture of MeOH (20 mL) and 6 N HCl aqueous solution (32 mL). The mixture was heated at 60 °C and stirred for 4 h. Then, the solvent was evaporated under reduced pressure. The crude product was washed with CHCl₃ and dried under high vacuum. Compound **C₂₀TACN** was obtained pure as a white solid (537 mg, 95%). ¹H NMR (CD₃OD, 500 MHz, 298 K): δ 0.91 (t, *J* = 6.9 Hz, 3H, CH₃), 1.29 (s, 34H, CH₂), 1.64 (s, 2H, CH₂), 2.85 (m, 2H, CH₂N), 3.10 (s, 4H, 2xCH₂N), 3.34 (m, 4H, 2xCH₂N), 3.55 (s, 4H, 2xCH₂N) ppm. ¹³C NMR (CD₃OD, 126 MHz, 298 K): δ 14.4, 23.7, 25.5, 28.3, 30.4, 30.5, 30.7, 33.0, 43.4, 44.6, 57.0, 66.0 ppm. HRMS (ES⁺) m/z calculated for C₂₆H₅₅N₃ [M+H]⁺ 410.4469, found 410.4470.

TEM and cryo-EM analysis. TEM images were recorded on a Jeol 300 PX electron microscope. Sample preparation without staining: one drop of a buffered aqueous solution (5 mM HEPES, pH 7.0) at the desired concentration was deposited on a TEM grid and dried under vacuum. Sample preparation with staining: first the grid was placed on a drop of sample solution for 1 min and then placed on a drop of 2% uranyl acetate solution for 1 min. The solvent was allowed to evaporate before imaging of the stained grid. For the cryo-EM, 3 μ L of sample were applied to Quantifoil holey carbon grids (copper Multi A, Quantifoil Micro Tools GmbH, Jena, Germany). Excess fluid was blotted from the grid for ~2 s with Whatman filter paper and then plunge frozen in liquid ethane using a home-made plunge freezer to achieve sample vitrification. Frozen samples were stored in liquid nitrogen until EM imaging. Vitrified samples were imaged using a CM200 FEG transmission EM (FEI, Eindhoven, the Netherlands) operated at 200 keV and equipped with a F224HD 2048x2048 CCD camera (TVIPS Gauting, Germany). EM images were acquired at 27,500x magnification (pixel size 0.602 nm), and at 12–18 μ m defocus.

AFM analysis. AFM samples were prepared by drop casting 50 μ L of a buffered aqueous solution (5 mM HEPES, pH 7.0) of **C₂₀TACN**·Zn²⁺ (100 μ M) on a silicon wafer (covered by a 380 μ m layer of native silicon dioxide). The analysis was carried out on an Agilent Technologies 5500 scanning probe microscope, operating in acoustic AC AFM mode (tapping mode) with a silicon Asylum Research high frequency cantilever displaying a resonance frequency of 318 kHz.

Confocal microscopy. Confocal images were acquired with a laser scanning confocal microscope (BX51WI-FV300-Olympus) coupled to a frequency doubled Ti:Sapphire femtosecond laser at 400 nm (VerdiV5-Mira900-F Coherent, 76 MHz repetition rate, 150 fs pulse duration). The

laser beam was scanned on a 40x40 μ m sample area with a 512x512 px resolution, using a 60x water immersion objective (UPLSAP060xW-Olympus). A longpass 435 nm filter was employed for the collection of C153 emission signal. For Fluorescence Correlation Spectroscopy (FCS) measurements, the laser beam was focused into the sample solution through the 60x objective. The emission signal, collected within the range 500–550 nm and focused on a 100 μ m optical fiber, was split by a 40/60 beam splitter into two avalanche photodiodes (MPD-PDM100). Time-correlated single photon counting method, supported by ultrafast electronics (PicoQuant-PicoHarp300), was employed for the calculation of the pseudo cross-correlation FCS curve. The acquisition time was set at 15–20 s to avoid the detection of intense signals from large aggregates.

FCS analysis. For the fitting of FCS curves of aggregates, a two-component free diffusion model was used:

$$G(\tau) = \frac{1}{N} \left[A \left(1 + \frac{\tau}{\tau_{D1}} \right)^{-1} \left(1 + \frac{\tau}{S^2 \tau_{D1}} \right)^{-1/2} + (1 - A) \left(1 + \frac{\tau}{\tau_{D2}} \right)^{-1} \left(1 + \frac{\tau}{S^2 \tau_{D2}} \right)^{-1/2} \right]$$

The first component (τ_{D1}) is assigned to the residual free C153 while the second one, shifted at longer lag times (τ_{D2}), is due to the inclusion of C153 into the hydrophobic part of the aggregate. *N* is the average probe number in the focal volume, *A* represents the relative contribution of free diffusion term with respect to the second longer contribution, and *S* is the laser beam shape factor ($S = z_0/\omega_0$). For the calibration of the focal volume in each measurement session, we used as fluorescent standard the C153 dye in HEPES buffer (100 nM). The diffusion coefficient of C153 (660 μ m² s⁻¹) has been calculated from the averaged rotational diffusion tensors over the three dimensions in “slip conditions”.^[41,59] The focal volume size (ω_0) was calculated from the relation between the diffusion coefficient (*D*) and the diffusion time (τ_D): $D = \omega_0^2/4\tau_D$. Due to different optical alignment, the size of ω_0 was 0.30 and 0.25 μ m for, respectively, **C₂₀TACN**·Zn²⁺ and **ATP**·**C₂₀TACN**·Zn²⁺ measurements. According to the Stokes-Einstein equation, the hydrodynamic probe radius (*r*) can be estimated from the following equation:

$$r = \frac{K_B T \times 4\tau_{D2}}{6\pi\eta\omega_0^2}$$

where η is the viscosity of the solution, *K_B* is the Boltzmann constant and *T* is the absolute temperature (293 K). As shown from TEM and cryo-EM micrographs, the structures formed by the addition of **ATP** are more similar to a sphere, while without the **ATP** the aggregates have a disk-like shape. For this reason, for FCS analysis of **C₂₀TACN**·Zn²⁺ sample, we approximated the disk-like shape to an ellipsoid having two identical dimensions (*a_x* and *a_y*) and one different dimension (*a_z*), with *a_z* << *a_x*, *a_y*. We used the equations reported in ref^[59] to estimate the radius of the equivalent sphere obtained by averaged rotational diffusion coefficient over the three dimensions. The principal components of the rotational diffusion tensor are: $D_i^{rot} = K_B T/f_i$, with *i* = x, y, z. *f_i* are the frictional coefficients that are simplified in the following expressions:

$$f_x = f_y = \frac{16\pi\eta(a_x^2 + a_z^2)}{3(a_x^2 P + a_z^2 R)}$$

$$f_z = \frac{16\pi\eta}{3P}$$

$$P = \int_0^\infty \frac{ds}{\sqrt{(a_x^2 + s)^4 (a_z^2 + s)}}; R = \int_0^\infty \frac{ds}{\sqrt{(a_x^2 + s)^3 (a_z^2 + s)^2}};$$

We combined resulting components as: $D_o^{rot} = 1/3 \sum_{i=1}^3 D_i^{rot}$ and used the definition of the rotational diffusion coefficient in “stick conditions” to

extract the expression for r , which is the radius of the equivalent sphere exposing the same surface area of the ellipsoid:

$$r = \sqrt[3]{\frac{K_B T}{8\pi\eta D_0^{Rot}}}$$

By substituting r in the expression of the translational diffusion and after some simplifications, D can be written as:

$$D = \frac{K_B T}{6\pi\eta r} = \sqrt[3]{\frac{(K_B T)^2 D_0^{Rot}}{27(\pi\eta)^2}} \equiv \frac{\omega_0^2}{4\tau_{D2}}$$

$$\sqrt[3]{\frac{(K_B T)^2 D_0^{Rot}}{27(\pi\eta)^2}} - \frac{\omega_0^2}{4\tau_{D2}} = 0$$

The ellipsoid dimensions a_x and a_z are found from the minimization of the last equation. Since the effect of a_z on the calculation is very poor (up to ~70–80 nm), we decided to fix a_z to 10 nm, in accordance with average disk-like micelles thickness measured by AFM analysis. The average size found for **C₂₀TACN·Zn²⁺** (100 μM) sample reported in the main text is calculated as $2a_x$. The size of **ATP/C₂₀TACN·Zn²⁺** (20/100 μM) aggregates is calculated from the standard Stokes-Einstein relation for a sphere reported above.

Synthesis of Au NP-MUA and Au NP-TACN·Zn²⁺. *Au NP-MUA.* A modified procedure from Stucky was adopted.^[65] 11-Mercaptoundecanoic acid (**MUA**, 44 mg, 202 μmol) and AuPPh₃Cl^[60,61] (50 mg, 101 μmol) were dissolved in THF (8 mL). *tert*-Butylamine borane complex (44 mg, 500 μmol) was then added as a powder and the reaction mixture was heated at 55 °C under vigorous mixing for 1 h and left gently cool at rt for further 5 h. The reaction was then quenched with Et₂O (8 mL) in order to achieve NP precipitation. The black solid was then washed twice with Et₂O by using the following procedure: NP were dispersed in the solvent (8 mL), sonicated for 15 min, and centrifuged. The same operation was performed in CH₂Cl₂ (8 mL) for three times. Evaporation under vacuum afforded Au NP-MUA as a black solid (28.7 mg). ¹H NMR (D₂O, 500 MHz, 295 K, Figure S23): the ¹H NMR of Au NP-MUA shows a pattern of broad peaks, characteristic of NP-bound molecular species. The absence of NP-unbound species was assessed by using a specifically developed CPMG-z pulse sequence to achieve T₂ filtering while avoiding signal distortion due to spin-spin coupling.^[62] When this pulse sequence is applied to a purified sample of Au NP-MUA, the broad signals corresponding to the NP-bound species are filtered out demonstrating that only signals originating from solvent are present. TEM, DLS, UV/Vis, TGA (Figure S24): the amount of NP-bound **MUA** was determined by TGA. A sample of purified Au NP-MUA (0.989 mg) lost 26.3% of its weight by TGA. Preparation of the stock solution of Au NP-MUA: a purified sample of NPs (19.8 mg) corresponds to 5.21 mg of NP-bound **MUA**. The black solid was dissolved in Milli-Q water (5 mL). Hence, [Au NP-MUA] = 4.78 μM or 1.04 mg mL⁻¹ in terms of **MUA**. *Au NP-TACN·Zn²⁺.* The procedure for the synthesis, purification and characterization, including the determination of the concentration of the NP-bound ligands can be found elsewhere in the literature.^[63]

Self-assembly between C₂₀TACN·Zn²⁺-stacked disks and Au NP-MUA or Au NP-TACN·Zn²⁺. *TEM analysis.* **C₂₀TACN·Zn²⁺** (100 μM) and **ATP** (20 μM) were mixed in aqueous buffered solution (HEPES pH 7.0, 5 mM) in the presence of CaCl₂ (0.25 mM). The mixture was left to equilibrate at rt for 24 h. Then, potato apyrase (final concentration: 1.5 U mL⁻¹) and Au NP-MUA or Au NP-TACN·Zn²⁺ (final concentration: 0–200 μM in terms of NP-bound ligand) was added and the mixture was incubated at 37 °C overnight. The solution was then left to cool to RT and

to equilibrate for further 24 h. Although no visible precipitation was observed, all solutions were gently shaken before the preparation of the TEM grid (no stain was used). *UV/Vis spectroscopy.* A solution containing **C₂₀TACN·Zn²⁺** (100 μM), **ATP** (20 μM), and CaCl₂ (0.25 mM) was left to equilibrate overnight. The mixture was then monitored by UV/Vis spectroscopy at 37 °C. After about 10 min from start, potato apyrase (1.5 U mL⁻¹) and Au NP-MUA (20 μM) were added to the mixture. A UV/Vis spectrum from 350 to 700 nm was recorded every 10 min for 8 h. The absorbance values at 534 nm (SPR band of Au NP-MUA) were plotted vs. time. The experiment was compared to a control where potato apyrase is absent. *DLS analysis.* The sample preparation is identical to that adopted for the UV/Vis analysis. After the addition of Au NP-MUA (20 μM), the hydrodynamic diameter of Au NPs was recorded every 15 min for 8 h.

Acknowledgements

Cryo-EM measurements were performed by E. Paccagnini and M. Gentile at the Electron Microscopy Laboratory of the Department of Life Sciences at the University of Siena directed by Prof. Dr. P. Lupetti.

Keywords: supramolecular chemistry • supramolecular amphiphiles • hierarchical self-assembly • surface functionalization

- [1] J.-M. Lehn, *Angew. Chem. Int. Ed.* **1988**, *27*, 89–112.
- [2] P. A. Gale, J. W. Steed, *Self-Assembly and Supramolecular Devices. Supramolecular Chemistry: From Molecules to Nanomaterials Vol. 5*, Wiley, **2012**.
- [3] G. M. Whitesides, E. E. Simanek, J. P. Mathias, C. T. Seto, D. Chin, M. Mammen, D. M. Gordon, *Acc. Chem. Res.* **1995**, *28*, 37–44.
- [4] L. J. Prins, D. N. Reinhoudt, P. Timmerman, *Angew. Chem. Int. Ed.* **2001**, *40*, 2382–2426.
- [5] A. Aggeli, I. A. Nyrkova, M. Bell, R. Harding, L. Carrick, T. C. B. McLeish, A. N. Semenov, N. Boden, *Proc. Natl. Acad. Sci.* **2001**, *98*, 11857–11862.
- [6] G. M. Whitesides, M. Boncheva, *Proc. Natl. Acad. Sci.* **2002**, *99*, 4769–4774.
- [7] P. Jonkheijm, P. van der Schoot, A. P. H. J. Schenning, E. W. Meijer, *Science* **2006**, *313*, 80–83.
- [8] Y. He, T. Ye, M. Su, C. Zhang, A. E. Ribbe, W. Jiang, C. Mao, *Nature* **2008**, *452*, 198–201.
- [9] X. Zhang, C. Wang, *Chem. Soc. Rev.* **2011**, *40*, 94–101.
- [10] S. J. Holder, N. A. J. M. Sommerdijk, *Polym. Chem.* **2011**, *2*, 1018–1028.
- [11] C. Wang, Z. Wang, X. Zhang, *Acc. Chem. Res.* **2012**, *45*, 608–618.
- [12] B. Gruber, B. König, *Chem. Eur. J.* **2013**, *19*, 438–448.
- [13] C. Rest, R. Kandanelli, G. Fernández, *Chem. Soc. Rev.* **2015**, *44*, 2543–2572.
- [14] J. P. Hill, W. Jin, A. Kosaka, T. Fukushima, H. Ichihara, T. Shimomura, K. Ito, T. Hashizume, N. Ishii, T. Aida, *Science* **2004**, *304*, 1481–1483.
- [15] T. Shimizu, M. Masuda, H. Minamikawa, *Chem. Rev.* **2005**, *105*, 1401–1444.
- [16] S. Yagai, M. Usui, T. Seki, H. Murayama, Y. Kikkawa, S. Uemura, T. Karatsu, A. Kitamura, A. Asano, S. Seki, *J. Am. Chem. Soc.* **2012**, *134*, 7983–7994.
- [17] A. V. Kabanov, V. A. Kabanov, *Adv. Drug Deliv. Rev.* **1998**, *30*, 49–60.
- [18] X. Hu, J. Hu, J. Tian, Z. Ge, G. Zhang, K. Luo, S. Liu, *J. Am. Chem. Soc.* **2013**, *135*, 17617–17629.

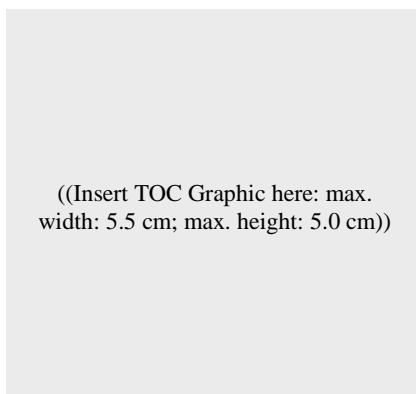
- [19] F. Mancin, P. Scrimin, P. Tecilla, U. Tonellato, *Coord. Chem. Rev.* **2009**, *253*, 2150–2165.
- [20] A. K uchler, M. Yoshimoto, S. Luginb uhl, F. Mavelli, P. Walde, *Nat. Nanotechnol.* **2016**, *11*, 409.
- [21] K. J. C. van Bommel, A. Friggeri, S. Shinkai, *Angew. Chemie Int. Ed.* **2003**, *42*, 980–999.
- [22] A. H. Gr schel, F. H. Schacher, H. Schmalz, O. V. Borisov, E. B. Zhulina, A. Walther, A. H. E. M uller, *Nat. Commun.* **2012**, *3*, 710.
- [23] H. Cui, Z. Chen, S. Zhong, K. L. Wooley, D. J. Pochan, *Science* **2007**, *317*, 647–650.
- [24] L. Yin, M. A. Hillmyer, *Macromolecules* **2011**, *44*, 3021–3028.
- [25] S. Venkataraman, A. L. Lee, H. T. Maune, J. L. Hedrick, V. M. Prabhu, Y. Y. Yang, *Macromolecules* **2013**, *46*, 4839–4846.
- [26] Z. Li, Z. Chen, H. Cui, K. Hales, K. Qi, K. L. Wooley, D. J. Pochan, *Langmuir* **2005**, *21*, 7533–7539.
- [27] J. Zhu, S. Zhang, K. Zhang, X. Wang, J. W. Mays, K. L. Wooley, D. J. Pochan, *Nat. Commun.* **2013**, *4*, 2297.
- [28] N. Kimizuka, T. Kawasaki, K. Hirata, T. Kunitake, *J. Am. Chem. Soc.* **1998**, *120*, 4094–4104.
- [29] R. Oda, I. Huc, M. Schmutz, S. J. Candau, F. C. MacKintosh, *Nature* **1999**, *399*, 566–569.
- [30] T. Gore, Y. Dori, Y. Talmon, M. Tirrell, H. Bianco-Peled, *Langmuir* **2001**, *17*, 5352–5360.
- [31] F. Garc a, F. Aparicio, M. Marenchino, R. Campos-Olivas, L. S anchez, *Org. Lett.* **2010**, *12*, 4264–4267.
- [32] M. N. Holme, I. A. Fedotenko, D. Abegg, J. Althaus, L. Babel, F. Favarger, R. Reiter, R. Tanasescu, P.-L. Zaffalon, A. Ziegler, et al., *Nat. Nanotechnol.* **2012**, *7*, 536.
- [33] F. Li, Q. Song, L. Yang, G. Wu, X. Zhang, *Chem. Commun.* **2013**, *49*, 1808–1810.
- [34] J. Hu, P. Wang, Y. Lin, S. Yang, B. Song, Q. Wang, *Org. Biomol. Chem.* **2014**, *12*, 4820–4823.
- [35] Y. Gong, T. Jiao, Q. Hu, N. Cheng, W. Xu, Y. Bi, L. Yu, *J. Phys. Chem. C* **2015**, *119*, 16349–16357.
- [36] C. Li, B. J. Cafferty, S. C. Karunakaran, G. B. Schuster, N. V. Hud, *Phys. Chem. Chem. Phys.* **2016**, *18*, 20091–20096.
- [37] F. Neuhaus, D. Mueller, R. Tanasescu, S. Balog, T. Ishikawa, G. Brezesinski, A. Zumbuehl, *Angew. Chem. Int. Ed.* **2017**, *56*, 6515–6518.
- [38] H. Cui, T. Muraoka, A. G. Cheetham, S. I. Stupp, *Nano Lett.* **2009**, *9*, 945–951.
- [39] J. A. Lehrman, H. Cui, W.-W. Tsai, T. J. Moyer, S. I. Stupp, *Chem. Commun.* **2012**, *48*, 9711–9713.
- [40] S. I. Stupp, R. H. Zha, L. C. Palmer, H. Cui, R. Bitton, *Faraday Discuss.* **2013**, *166*, 9–30.
- [41] S. Maiti, I. Fortunati, C. Ferrante, P. Scrimin, L. J. Prins, *Nat. Chem.* **2016**, *8*, 725–731.
- [42] J. B. F. N. Engberts, J.-J. H. Nusselder, *Pure Appl. Chem.* **1990**, *62*, 47–55.
- [43] X. Zhang, J. K. Jackson, H. M. Burt, *J. Biochem. Biophys. Methods* **1996**, *31*, 145–150.
- [44] A. Diller, C. Loudet, F. Aussenac, G. Raffard, S. Fournier, M. Laguerre, A. Gr elard, S. J. Opella, F. M. Marassi, E. J. Dufourc, *Biochimie* **2009**, *91*, 744–751.
- [45] J. N. Israelachvili, D. J. Mitchell, B. W. Ninham, *J. Chem. Soc. Faraday Trans. 2, Mol. Chem. Phys.* **1976**, *72*, 1525–1568.
- [46] L. M. S. Loura, J. P. Prates Ramalho, *Biophys. Rev.* **2009**, *1*, 141–148.
- [47] J. L.-Y. Chen, S. Maiti, I. Fortunati, C. Ferrante, L. J. Prins, *Chem. Eur. J.* **2017**, *23*, 11549–11559.
- [48] C. Pezzato, L. J. Prins, *Nat. Commun.* **2015**, *6*, 7790.
- [49] M. Haruta, M. Dat e, *Appl. Catal., A* **2001**, *222*, 427–437.
- [50] N. Dimitratos, J. A. Lopez-Sanchez, G. J. Hutchings, *Chem. Sci.* **2012**, *3*, 20–44.
- [51] A. N. Shipway, E. Katz, I. Willner, *ChemPhysChem* **2000**, *1*, 18–52.
- [52] C. N. R. Rao, G. U. Kulkarni, P. J. Thomas, P. P. Edwards, *Chem. Soc. Rev.* **2000**, *29*, 27–35.
- [53] J. N. Anker, W. P. Hall, O. Lyandres, N. C. Shah, J. Zhao, R. P. Van Duyne, *Nat. Mater.* **2008**, *7*, 442.
- [54] F. Li, D. P. Josephson, A. Stein, *Angew. Chem. Int. Ed.* **2011**, *50*, 360–388.
- [55] N. Zheng, J. Fan, G. D. Stucky, *J. Am. Chem. Soc.* **2006**, *128*, 6550–6551.
- [56] L. J. Prins, *Acc. Chem. Res.* **2015**, *48*, 1920–1928.
- [57] M. Diez-Castellnou, F. Mancin, P. Scrimin, *J. Am. Chem. Soc.* **2014**, *136*, 1158–1161.
- [58] S. Kimura, E. Bill, E. Bothe, T. Weyherm uller, K. Wieghardt, *J. Am. Chem. Soc.* **2001**, *123*, 6025–6039.
- [59] Y. E. Ryabov, C. Geraghty, A. Varshney, D. Fushman, *J. Am. Chem. Soc.* **2006**, *128*, 15432–15444.
- [60] D. M. L. Goodgame, C. A. O'Mahoney, S. D. Plank, D. J. Williams, *Polyhedron* **1993**, *12*, 2705–2710.
- [61] T. E. M uller, J. C. Green, D. M. P. Mingos, C. M. McPartlin, C. Whittingham, D. J. Williams, T. M. Woodroffe, *J. Organomet. Chem.* **1998**, *551*, 313–330.
- [62] F. Rastrelli, S. Jha, F. Mancin, *J. Am. Chem. Soc.* **2009**, *131*, 14222–14224.
- [63] G. Pieters, A. Cazzolaro, R. Bonomi, L. J. Prins, *Chem. Commun.* **2012**, *48*, 1916–1918.

Entry for the Table of Contents (Please choose one layout)

Layout 1:

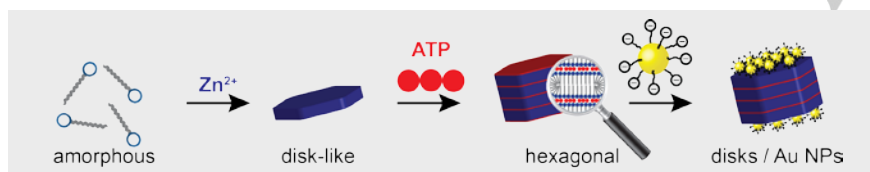
FULL PAPER

Text for Table of Contents

*Author(s), Corresponding Author(s)****Page No. – Page No.****Title**

Layout 2:

FULL PAPER

*F. della Sala, W. Verbeet, S. Silvestrini, I. Fortunati, C. Ferrante and L. J. Prins****Page No. – Page No.****Stepwise Hierarchical Self-Assembly of Supramolecular Amphiphiles into Higher-Order Threedimensional Nanostructures**

Controlled multistep self-assembly is achieved by a series of consecutive processes relying on noncovalent interactions only. The process starts with the formation of a metallo-surfactant *via* complexation of Zn²⁺-ions by the amphiphile forming disk-like micelles. Upon the addition of ATP these disks stack on top of each other to yield extraordinary large 3D hexagonal prisms. Eventually, these stacked disks can be functionalized with negatively charged gold nanoparticles through an enzyme-controlled self-assembly process.